

Feature Article

Simulation of Print Quality Defects*

Woonyoung Jang^{▲†} and Jan P. Allebach[†]*School of Electrical and Computer Engineering Purdue University West Lafayette, Indiana, USA*

Simulation of print quality (PQ) defects is the process of artificially adding structures to an image that when printed will have the appearance of real artifacts. Simulated PQ defects can be used in a variety of types of diagnostic printer documentation, in the development of test pages for PQ defect diagnosis, in the investigation of the perception of PQ defects, and in the development of algorithms for autonomously identifying PQ defects. We develop a general framework for PQ defect simulation, and apply it to the simulation of three different classes of PQ defects associated with color laser printers: defects of uniformity, random marks or repetitive artifacts, and color defects. Each defect is simulated by a geometrical model, or by a scanned sample prototype. The parameters of the model are estimated from actual PQ defect samples. We demonstrate the capability to generate photo-realistic simulations of a total of 9 different defects.

Journal of Imaging Science and Technology 49: 1–18 (2005)

Introduction

Print quality (PQ) defects of laser printers are artifacts that degrade the quality of printed images, which are generated by the electrophotographic process and/or print mechanism. The simulation of print quality defects is a process in which an image is degraded by artificially generated structures to create an impression of real defects when the image is viewed or printed. Why simulate PQ defects? In fact, there are a number of reasons why simulation of PQ defects is of considerable benefit. In an increasingly competitive marketplace, improvement of service and support processes is an important way for a manufacturer to increase profitability. This problem can be attacked on three fronts: (1) improve communication between the customer and the call center agent, (2) enable the customer to resolve the problem on his or her own, and (3) provide the capability to autonomously determine the cause of the issue. PQ defect simulation has a role to play in all three of

these areas. Resolution of PQ defect issues is among the most challenging of support problems because of the difficulty of providing an unambiguous description of the PQ defects. A representative image of the defect is one of the most effective ways to do this.

These images are typically generated either from an illustrator's rendering of the defect, or by scanning a print that contains the defect. The illustrator's rendering is often too simplistic to effectively convey the appearance of the defect in an actual print. The scanning based approach also has limitations. First, because of the low contrast and/or fine structure of the PQ defect, scanning may not capture well its characteristics. Second, the content of the page on which the defect occurs may confound the customer's understanding of what the defect looks like. For example, a defect consisting of repeated vertical bands may be printed on a page used for testing in the manufacturer's laboratory that consists of vertical blocks with different colors. The customer may have trouble differentiating between the features of the defect and those of the test page. Third, the best example of the defect may be observed on content provided by a customer through a beta test program or as part of issue resolution shortly after the product is introduced in the marketplace. For reasons of confidentiality, this example may not be useable to illustrate the PQ defect.

Simulation of the PQ defect based on characterization and modeling of the defect overcomes all these problems. The defect can be placed on any image content that is desired. This content can be chosen to make the defect most visible and unambiguous. The defect can be modified to maintain a consistent appearance across different formats: an image at an on-line support site that is viewable in a web browser, a full page print sample provided in a training class for service technicians, a figure in the user's manual for the product, or a thumbnail in a table cataloging a set of possible defects.

Original manuscript received December 22, 2003

▲ IS&T Member

◆ IS&T Fellow

*Research supported by the Hewlett-Packard Company

†Corresponding Author: W. Jang, woonyoung.jang@hp.com

Supplemental Material—Figures 6, 9, 16, 27, 29, 34, 39, 42, 43, and 47 can be found in color on the IS&T website (www.imaging.org) for a period of no less than two years from the date of publication.

©2005, IS&T—The Society for Imaging Science and Technology

PQ defect simulation is also an important tool for research and development. The design of test pages to aid the user in identifying PQ defects¹ is aided considerably by the capability to simulate how print quality defects would appear on these pages. In order to study the perception of a particular PQ defect, it is important to be able to present it to the observer at a number of different levels of strength and in the presence of a number of different image contents.^{2,3} Finally, development of algorithms for automatic detection and identification of PQ defects⁴ similarly requires the capability to provide a number of different instantiations of each defect.

PQ defects can be caused by the non-ideal characteristics of the marking process and print mechanism or by a damaged or contaminated printer component. We consider nine print defects as they are most commonly encountered in prints from laser printers: fine pitch banding, scan axis streaks, randomly scattered white specks, toner bubble marks, repetitive marks, repetitive coarse-pitch bands, ghosting, color plane registration error, and temporal color inconsistency. These defects may be categorized into three groups in terms of spatial characteristics and/or simulation methods: 1) defects of uniformity, 2) random marks or repetitive artifacts, and 3) color defects. The defects in the first group produce visible density variations appearing as fine pitch banding or scan axis streaks in constant tone areas. The second group has two different types: one is random and the other is repetitive. The former appears as randomly distributed dots or smudges, while the latter shows repetitive marks with a fixed interval. While defects of the first and second groups may be characterized by unique spatial features such as localized marks, or fine pitch banding that occurs throughout halftone areas, not all defects in the third group have distinctive spatial characteristics. For example, poor color consistency is manifest by an overall shift in the color rendering of a page. Another common defect belonging to this group is a failure of color plane registration, which is most often noticed as a halo or shadowing around text. While this is a spatial effect, its geometry is determined by the image context and not by the defect itself.

The defects of uniformity are indigenous to the marking process and print mechanism associated with laser printer, and are seen to varying degrees with all laser printers. Thus, these defects have been especially widely studied. Fine pitch banding has been investigated by using Fourier analysis,^{5,6} and characterized by using a first-order geometry-based printing model,⁷ or a 1D periodic signal model.⁸ Researchers have found that a major cause of fine pitch banding is the velocity fluctuations of the optical photoconductor (OPC) drum, which results in non-uniform line spacing.^{5,7,9,10} Another defect of this group is scan axis streaks, which are not periodic but rather are isolated and randomized in occurrence. Isolated streaks have been simulated with a Gaussian profile, and randomized streaks have been simulated using a $1/f$ noise model,¹¹ Both fine pitch banding and scan axis streaks have been quantified by developing a spectral separation technique to estimate individual noise power spectra.⁸

Randomly scattered specks and repetitive marks are common PQ defects which belong to the second group. These two defects can be differentiated from each other by their spatial distribution. Ghosting is also considered to be a PQ defect in this group by virtue of its repetitiveness. The causes of ghosting have been identified and a method presented to analyze it in the frequency

domain by using a ghosting test target page.¹² Perceptual measurement of ghosting has also been based on psychophysical experiments.¹³

Other than PQ defects or artifacts associated with laser printers, film graininess has been simulated for a range of severities and used in a ruler for measurement of graininess by visual inspection.¹⁴ In the medical imaging area, tumors have been simulated by using a Gaussian radial profile and superimposed on clinical gamma ray images to test a tumor detection system.¹⁵ Also, a framework for modeling and predicting anatomical deformations has been presented and tested on simulated images.¹⁶ In this work, training samples were used to statistically model the shape of the deformation. Finally, the shape of lesions has been modeled and simulated in computer tomography images; and the simulated data have been used to develop a computer-aided algorithm that detects colonic polyps and lung nodules.¹⁷

We can categorize the approaches for the modeling of imaging defects or artifacts into two groups. One is to model the imaging system which generates the defects, and the other is to model the imaging defects themselves based on their own characteristics, while considering the imaging system as a black box.

In the first approach, the imaging system is modeled and characterized in a framework that specifies the relationship between the artifact quantified by the physical image parameters and the corresponding system parameters. For example, the image capture system can be modeled in terms of its components such as the collecting optics, image sensors, and other associated mechanical and/or electrical devices. Then the physical parameters of the artifact such as noise and blur,¹⁸⁻²⁰ and optical aberrations^{21,22} are modeled and characterized and associated with appropriate sub-systems in the system modeling process. These models can be used as the basis for correcting distortions, enhancing image quality, and simulating artifacts. For example, in the domain of printing, the electrophotographic process has been modeled in terms of the laser beam intensity profile, exposure of the organic photoconductor, and the resulting absorbance on the paper. This model has then been embedded into the direct binary search halftoning algorithm.²³

On the other hand, the second approach considers the imaging system as a black box. It can be extremely difficult to accurately model the process whereby malfunctions in an imaging system generate defects. In this case, we can characterize the defect by extracting its profile and analyzing the relevant physical image parameters such as tone dependency, spatial distribution, or geometrical shape of the defect, without directly specifying the characteristics of the system that gave rise to the corresponding defect.

Although considerable research has been devoted to analyzing many types of image quality artifacts and PQ defects, little attention has been paid to simulating the PQ defects. In this article, we characterize a set of PQ defects which are common in color laser printers. These defects can be observed with both multipass and in-line laser printers. Except as noted, the appearance of each defect is not specific to either printer architecture.

The printer system which generates a defect can be modeled and simulated in hardware. For example, laser printing systems have been modeled to analyze and reduce fine pitch banding by controlling a system parameter which is the velocity of the optical photoconductor.^{9,24} Also fine pitch banding has been modeled and simulated, and its strength has been measured by psychophysical experiments which provides the perceptual goodness of

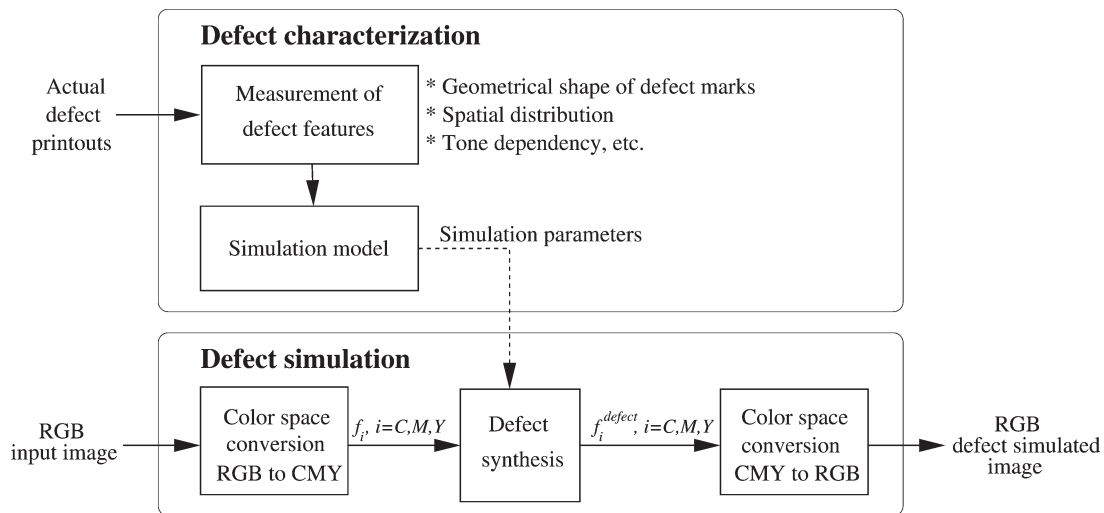


Figure 1. General framework for the characterization and simulation of PQ defects. This procedure is common to all the defects described in this article.

image quality (or badness of the defect) as a function of physical image parameters.³ However, only one defect is modeled and simulated in each of the Refs. 3, 9 and 24. Instead of modeling one defect by relating perceptual goodness to a system parameter, we use a general approach to characterize and simulate various types of PQ defects in this article.

Based on the measurement and characterization of each defect, we describe a simulation procedure for adding the defect to a continuous tone image. Aside from the solutions developed for the specific PQ defects considered in this article, we describe a general framework for PQ defect simulation, and illustrate the application of a range of tools from signal processing, geometry, and stochastic modeling to the simulation of PQ defects. Except as noted, we consider for simplicity only the case of a three color printer, although the concepts discussed herein may readily be extended to the four-color case.

The rest of the article is organized as follows. In the next section, we describe a general framework for characterization and simulation of PQ defects. Following that, we discuss how to simulate defects of uniformity. Then, we present methods for simulating the defects of random marks and repetitive artifacts. Finally, we describe the procedure for simulating color defects. In this article, we will use the letters C, M, and Y to denote the colors of cyan, magenta, and yellow, respectively.

General Framework for Simulation of PQ Defects

To simulate a defect in a continuous tone image with arbitrary content, we perform the following steps. First, we characterize the defect by measuring its features such as the shape and spatial distribution of the defect marks, or tone dependency of the defect. We measure the features from images captured by scanning prints containing the defect. This approach may appear to contradict our earlier discussion of the weakness of using scanned samples of PQ defects, which may result in a poor quality defect reproduction. Our approach here is to parameterize or obtain a prototype of the defect, which is faint in many cases. This allows us the flexibility to modify the contrast or distinctiveness of the defect for further defect reproduction. Also, by extracting the prototype of the defect from the scanned sample, we can incorporate the defect onto an arbitrary background.

In our work, we use a flatbed scanner (Heidelberg Saphir Ultra2: Heidelberg USA, Inc., Kennesaw, GA 30144) and convert the scanner values to units of absorbance via a scanner calibration curve. We then build a simulation model for the defect based on the measurements. The model specifies a simulation procedure which shows how to synthesize the defect within a continuous tone image. The simulation model also contains a set of simulation parameters to control the severity of the defect. Most of the defects belonging to the first and second groups require a defect profile which is synthesized in an input image during the simulation process. A defect profile is generally described by its geometrical shape and/or the absorbance variation of the defect.

There are two different approaches to generating a defect profile. The first is the stochastic model based approach, and the second is the prototype sample based approach. The first approach characterizes an entire ensemble of scanned defect samples by extracting prominent features from these samples. Those features are characterized in terms of the parameters of a geometrical model. This allows us to capture the natural variation in the appearance of the defects across the page. However, it is difficult to model the geometrical shape of some defects, especially if the shape of the defect mark is very complex or we cannot collect a sufficient number of defect samples to support a statistical analysis. In our study, we use the stochastic model based approach to simulate the defects of randomly scattered white specks, toner bubble marks, and repetitive coarse-pitch bands, all of which are described in the *Simulation of Random Marks and Repetitive Artifacts* section.

On the other hand, the second approach uses a defect prototype which we generate from a scanned image of an actual defect sample. Since we can generate an accurate defect profile from one real defect sample by using this approach, it may be considered to be a desirable approach when we have only one or a limited number of defect samples. However, we have no basis for generating other profiles in the simulation process than those captured as defect prototypes. This may result in lack of representativeness; so a simulated defect may look very different from what users may encounter in the field. We use the prototype sample-based approach to simulate fine pitch banding and scan axis streak defects which we describe in the *Simulation of Defects of*

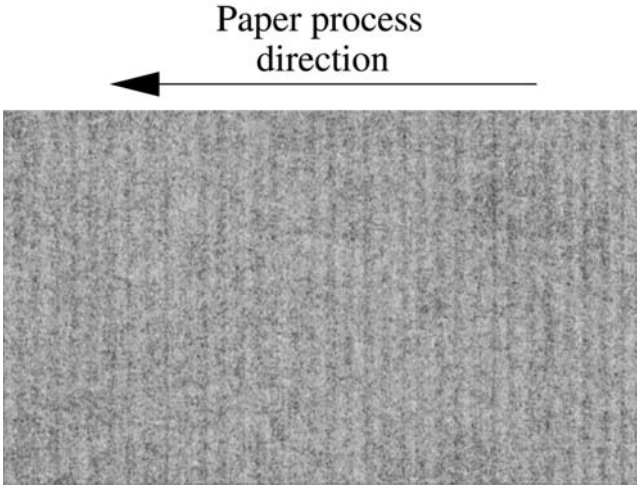


Figure 2. A scanned sample of the banding defect.

Uniformity section, and to simulate the defect of repetitive marks described in the *Simulation of Random Marks and Repetitive Artifacts* section.

The block diagram in Fig. 1 depicts the general framework for the characterization and simulation procedure, which is common to all the defects described in this article. The input to this simulation process is an RGB continuous tone image, which is converted into a CMY continuous tone image. Since the simulation methods described in this article are not specific to a particular printer, we use the simple transformation from RGB space to CMY space given by

$$[C M Y]^t = [1 1 1]^t - [R G B]^t, \quad (1)$$

where $0 \leq R, G, B \leq 1$, and the superscript t denotes transpose. We can easily replace this by the transformation for a particular printer, if desired. After the color space conversion, we separately synthesize the defect features for each of the CMY color planes. Finally we convert back to RGB. In this article, we will use the term normalized digital value to indicate the CMY color value $a_i \in [0, 1]$, $i = C, M$, and Y . We will omit the subscript when there is no possibility of confusion.

Simulation of Defects of Uniformity

The defects of uniformity are print artifacts that are easily noticed in nominally uniform areas. In this section, we will show how to simulate fine pitch banding and scan axis streaks, which are very common defects of laser printers.

Fine Pitch Banding

In an electrophotographic laser printer, a laser beam is scanned across the surface of an OPC drum in a direction perpendicular to the motion of the OPC drum. Since the velocity of the OPC drum generally varies with time, its vibratory motion causes the raster lines on the surface of the drum to be unevenly spaced.^{7,9} These raster position errors result in density variation in the paper process direction, which appears as tightly packed lines as shown in Fig. 2.

Banding is more prominent at certain tone levels than at others. We developed a measurement method for characterizing this tone dependency. We obtain the Banding Tone Dependency Function (BTDF) by the following steps:

1. A test target page consisting of solid bars at twenty different normalized digital values ($a = 0.05, 0.10, 0.15, \dots, 1.00$) is generated and saved in TIFF file format. The size of each bar is $5.4 \text{ in} \times 0.5 \text{ in}$.
2. We print ten test target pages from a laser printer using the halftone technique provided by the printer driver.
3. We scan the printed test target pages at 600 dpi, and crop each test bar to avoid edge effects. We then convert the scanner values to absorbance values by using a scanner calibration curve.
4. For a given tone a , we obtain the 1D segment $g_a^{(l)}[n]$ by averaging each column of scanned data $g_a^{(l)}[m, n]$ perpendicular to the paper process direction as

$$g_a^{(l)}[n] = \frac{1}{M} \sum_{m=1}^M g_a^{(l)}[m, n], \quad (2)$$

- where M is the number of points per segment perpendicular to the paper process direction, and l is the bar index which represents the test target page number out of ten pages in this measurement. We call this segment the *projected absorbance profile*.
5. From $g_a^{(l)}[n]$, we compute a periodogram²⁵ as

$$P_a^{(l)}(v) = \frac{1}{N} \left| \sum_{n=0}^{N-1} g_a^{(l)}[n] e^{-j2\pi vn/N} \right|^2, \quad (3)$$

where N is the number of points per segment parallel to the paper process direction, and l is the segment index. Then we obtain a power spectrum estimate $S_a(v)$ by using Bartlett's method,²⁵ which averages the periodograms for L segments as

$$S_a(v) = \frac{1}{L} \sum_{l=1}^L P_a^{(l)}[v]. \quad (4)$$

6. For a given tone a , we calculate the power $E(a)$ from the power spectrum estimate $S_a(v)$ over a certain frequency range which is considered to be associated with banding.
7. The *spline* function in MATLAB (The MathWorks, Inc. Natick, MA) yields the interpolated curve $\hat{E}(a)$ from the measured data points $E(a)$, $a = 0.05, 0.10, \dots, 1.00$. This *spline* function is used to interpolate all data sets in the remainder of this article.
8. Normalizing the square root of $\hat{E}(a)$ we obtain the BTDF

$$h^b(a) = \frac{\sqrt{\hat{E}(a)}}{\max_{0 \leq a \leq 1} \sqrt{\hat{E}(a)}}, \quad a \in [0, 1]. \quad (5)$$

Figure 3 shows the projected absorbance profiles and their spectra at three different tone levels for the black plane. We note that the profile for the midtone level ($a = 0.5$) shows larger fluctuation than that for a lighter tone level ($a = 0.25$) or a darker tone level ($a = 0.75$). This fact is reflected in their power spectra shown in the lower row of Fig. 3, where several major banding frequencies appear. In our experiment, we calculated the power for the frequency range $[5, 90]$ cycles/in which contains most of the major banding frequencies, and used that power to obtain a tone dependency function. The resulting BTDF for the black plane is shown in Fig.

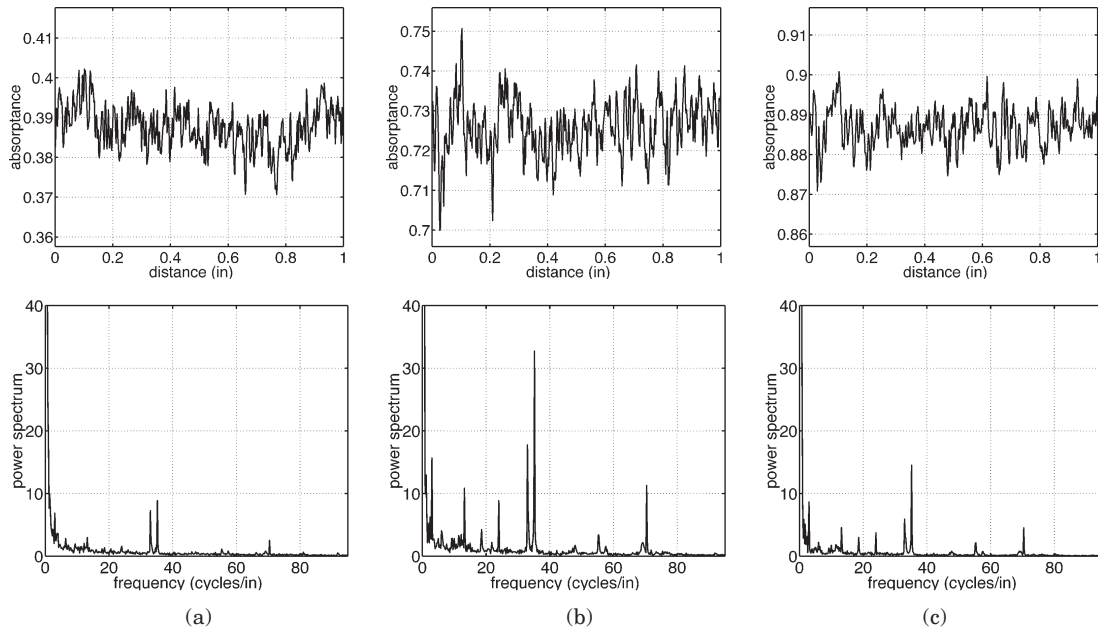


Figure 3. Projected absorptance profiles for the K plane and their spectra for the nominal absorptance levels (a) $a = 0:25$, (b) $a = 0:50$, and (c) $a = 0:75$.

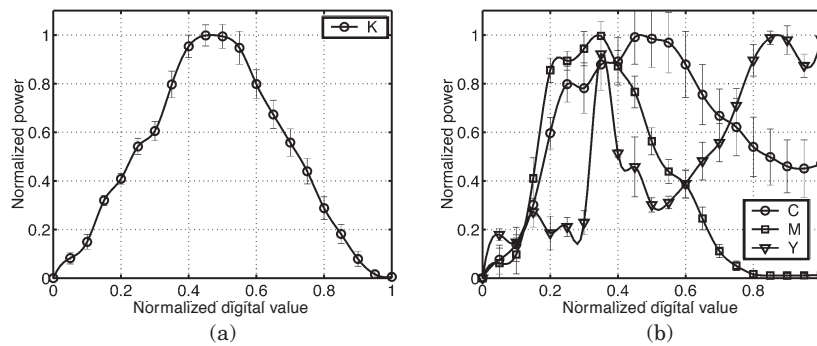


Figure 4. Measurement of banding tone dependency for (a) K plane, and (b) CMY planes. The ratio of the maximum power for these color planes is $K:C:M:Y = 1:0.80:0.87:0.29$. Each error bar shows ± 1 standard deviation of the measurements that were averaged to obtain the corresponding data point.

4(a). By utilizing the BTDF obtained above, we build a banding simulation model for a monochrome image as

$$f_i^{banding}[m, n] = f_i[m, n] + \rho_i h_i(f_i[m, n]) d_i[n], i = C, M, Y, (6)$$

where $f_i[m, n]$ is the input image, ρ_i is a parameter controlling the overall defect level, $h_i(\bullet)$ is the tone dependency function, and $d_i[n]$ is a prototype defect signal weighted by the tone dependency function.

Following the prototype sample based approach, we generate a banding signal by using a sample projected absorptance profile obtained from a printed patch with absorptance corresponding to the peak in the BTDF, and process it to retain the frequency range which is considered to be associated with banding. We utilize an ideal bandpass filter which has unit magnitude response in this interval and zero response elsewhere. The passband of the filter that we used is $[5, 90]$ cycles/in, which is the same frequency range used to obtain the BTDF. We can extend this method to the banding simulation for color images by using separate BTDF's and banding signals for each of the CMY planes. The BTDF's and banding

signals for the CMY planes are measured and obtained as described above. The resulting banding tone dependency for the CMY color planes is shown in Fig. 4(b).

The general framework introduced in Fig. 1 is used in the simulation of banding. Figure 5 shows the defect synthesis block in detail. The input to the block is a CMY color image. Each color plane is separately processed according to Eq. (6). The banding simulation result is shown in Fig. 6, where banding appears as closely spaced vertical lines.

Scan Axis Streaks

Scan axis streaks are another type of defect of uniformity that are easily observed in a constant tone area. Streaks are a unidirectional defect that can be characterized by a 1D additive signal^{8,11,26} in a manner similar to that for fine pitch banding. However, the appearance of streaks is different than that of fine pitch banding. While fine pitch banding appears as tightly packed periodic lines perpendicular to the paper process direction, the streak defect has rather irregular and wider lines in the paper process direction as shown in Fig.

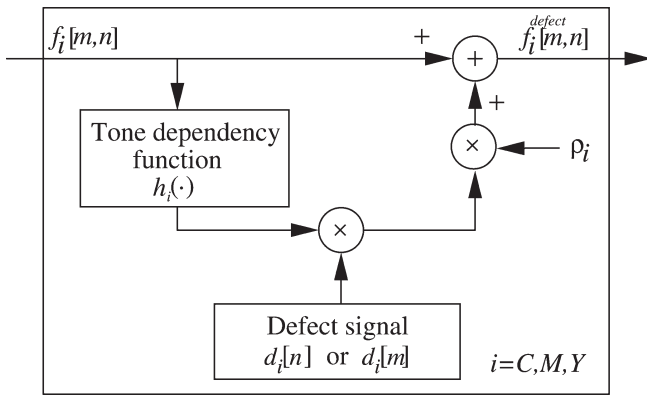


Figure 5. Defect synthesis block for banding and streaks.

7(a). Figure 7(b) shows the projected absorbance profile for the streak defect. The strength of the streak defect also depends on the tone level. Thus we consider the tone dependency of streaks in the simulation process, as we do when simulating the fine pitch banding defect. We then model the streak simulation by using Eq. (6) with a slight change to the index of the defect signal. Since the direction of the streak defect is perpendicular to that of the fine pitch banding defect, we use $d[m]$ instead of $d[n]$ for the streak simulation.

We generate the prototype streak signal in a way similar to that used to obtain the prototype fine pitch banding signal. We filter the projected absorbance profile to retain a frequency range which is considered to be associated with the streak defect. The frequency interval that we chose is [1, 35] cycles/in. Figure 7(c) shows the prototype streak signal which we obtain by filtering the absorbance profile in Fig. 7(b). We incorporate the tone dependency of the streak into the simulation procedure by measuring the spectra of streaks at various tone levels and defining the STDF which plays the same role as does the BTDF in banding simulation. We obtain the STDF by following steps similar to those used to generate the BTDF. However, we note that the direction of the streak defect is perpendicular to that of the fine pitch banding defect so the projected absorbance profiles are obtained in the perpendicular direction too. Figure 8(a) shows the streak tone dependency for the black plane measured at ten different tone levels.

As was done with the fine pitch banding simulation, we extend this method to streak simulation for color images by using separate STDF's and streak signals for the CMY planes. The measured streak tone dependency for the CMY color planes is shown in Fig. 8(b). The defect synthesis block for streak simulation in a color input image is the same as that for the fine pitch banding simulation shown in Fig. 5. A streak simulation image is shown in Fig. 9, where irregular horizontal lines appear.

Simulation of Random Marks or Repetitive Artifacts

The PQ defects described in the previous section are distributed over the entire image, and lack distinct boundaries. In this section, we will discuss defects that are more localized. For some of them, the marks are randomly scattered across the page. Others appear in a repetitive pattern. We will present simulation procedures for five defects belonging to this second defect group: randomly scattered white specks, toner bubble

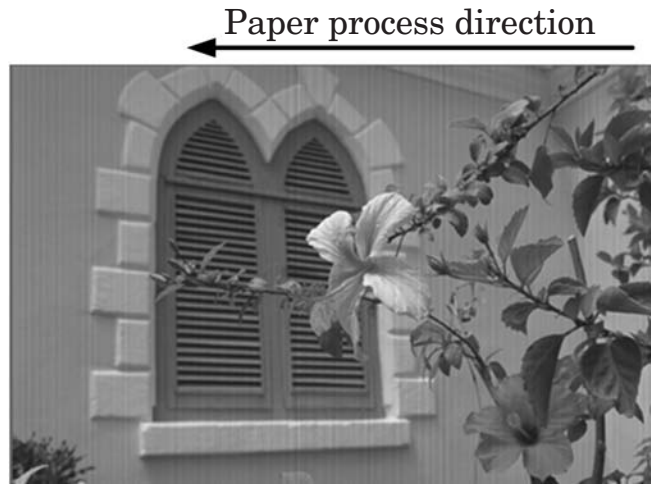


Figure 6. Image with simulated banding defect. Banding appears as closely spaced vertical lines. *Supplemental Material—Figure 6 can be found in color on the IS&T website (www.imaging.org) for a period of no less than two years from the date of publication.*

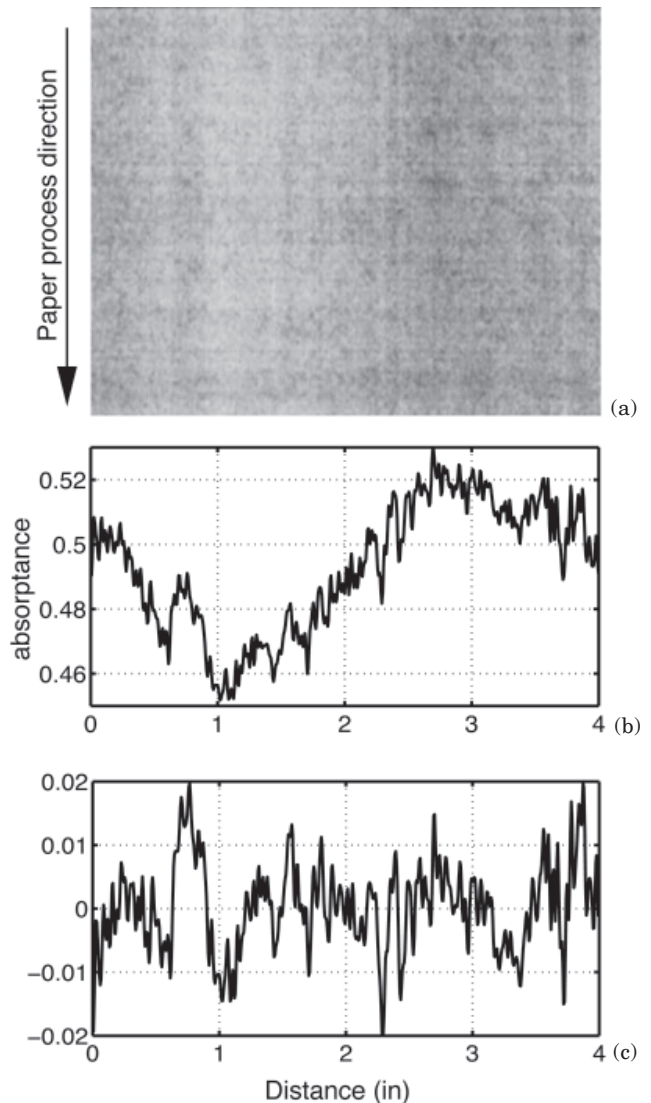
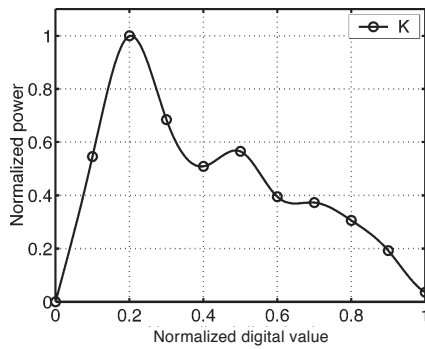
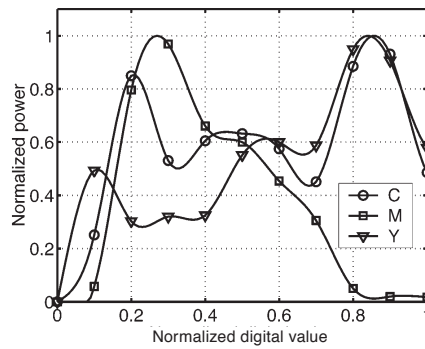


Figure 7. (a) A scanned sample of the streak defect, (b) its absorbance profile, and (c) a prototype streak signal acquired from (b). The streak signal is obtained by altering the projected absorbance shown in (b).



(a)



(b)

Figure 8. Measurement of streak tone dependency for (a) K plane, and (b) CMY planes. The ratio of the maximum power for these color planes is K:C:M:Y = 1: 0.74: 1.97: 0.18.

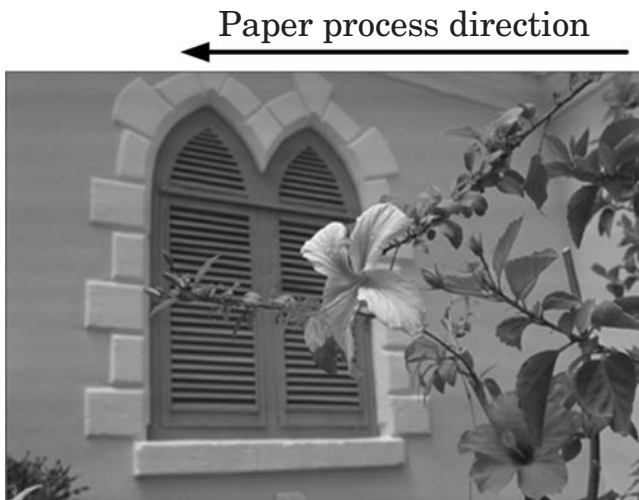


Figure 9. Image with simulated streak defect. The streaks appear as irregular horizontal lines. Here the cyan plane was assumed to be defective in the simulation process. *Supplemental Material—Figure 9 can be found in color on the IS&T website (www.imaging.org) for a period of no less than two years from the date of publication.*

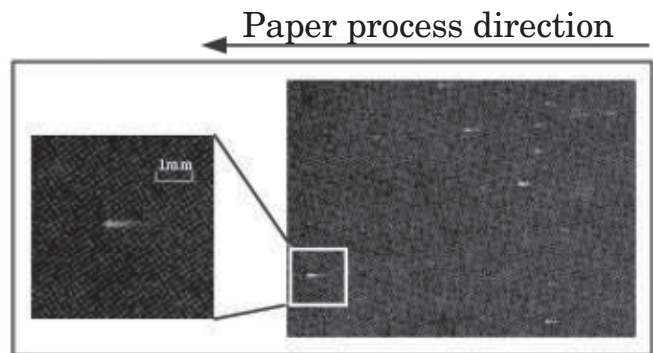


Figure 10. Scanned sample of scattered white specks.



Figure 11. Samples of white speck defects.

marks, repetitive marks, repetitive coarse-pitch bands, and ghosting.

Randomly Scattered White Specks

During the course of normal operation, foreign matter may accumulate at various points within the printer. If such material adheres to the OPC and cannot be removed during normal cleaning, it will prevent development at the points where the contaminant is located. For a multipass architecture in which the same OPC drum is used for all four colorants, this problem will occur at the same position in all four color planes. As a result, scattered small white specks will appear on the print as shown in Fig. 10.

We used a test target page which has a 100% black field of size 7 in \times 10 in. We printed the test target page on a printer with a contaminated OPC drum. We scanned the printed test target page at 1200 dpi, and cropped it to 6 in \times 9 in to retain only the black field area. We then segmented separately each white speck in the scanned test target page. We segmented a total of 589 white specks. A few samples of these white specks are shown

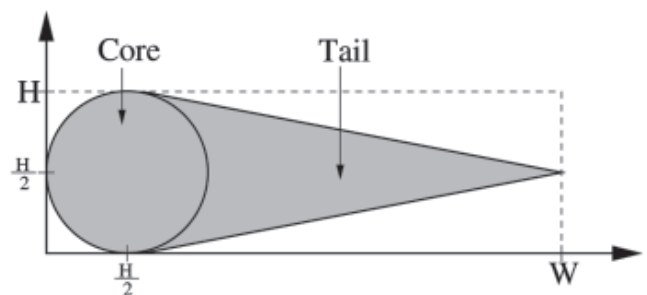


Figure 12. Modeling the shape of the white speck. The model consists of separate core and tail components.

in Fig. 11. We observe that the white specks are horizontally elongated, and have a tail-like area which fades out. Based on this inspection, we model the white speck as shown in Fig. 12. According to this model, each white speck is specified by two parameters: its width W and height H .

In the scanned test target image, we measured the width and height of each segmented speck. Then we sta-

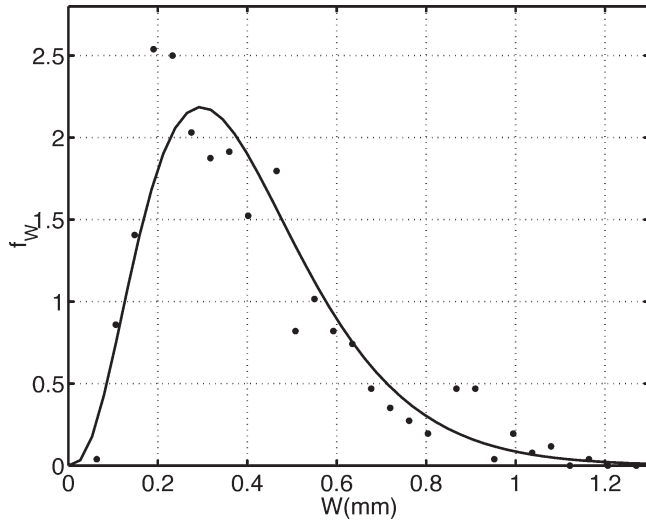


Figure 13. Sample probability density of the width W of a white speck with fitted Gamma density function ($\alpha = 3.79$, $\beta = 0.106$).

tistically analyzed the distributions of W and H . First, we inspected the distribution of W shown in Fig. 13, and fitted to the data a Gamma distribution with two parameters α and β ,

$$f(x|\alpha, \beta) = \frac{1}{\beta^\alpha \Gamma(\alpha)} x^{\alpha-1} e^{-\frac{x}{\beta}}. \quad (7)$$

We estimated α and β by using a maximum likelihood (ML) estimator. For a given W , we used a linear regression to find H by exploiting the relationship between the distribution of H and that of W .

We also examined the spatial distribution of the white specks on the printed test target page, shown in Fig. 14. The correlation coefficient of the horizontal position X and the vertical position Y is -0.02 . Since they are not highly correlated, we separately inspected the distribution of the horizontal and vertical positions of the white specks. As shown in Fig. 14(b), the vertical distribution of the white specks has a bell shape that is well fitted by a Gaussian function. On the other hand, the horizontal distribution of the specks is rather irregular and exhibits no particular shape; so we simply model it as a uniform density function, as shown in Fig. 14(c).

Figure 15 shows the defect synthesis block for randomly scattered white specks and repetitive marks. For each white speck, random parameters W , H , X , and Y for its size and position are generated based on the distributions described above. The shape of the white speck is then based on the model depicted in Fig. 12. The white speck is placed in the input image by setting the digital values of the corresponding pixels of the CMY planes to zero. This can be done by using the min operator and a defect mask which has zeros where the white specks are located and ones elsewhere. Figure 16 shows the resulting randomly scattered white specks in a continuous tone image.

Toner Bubble Marks

Toner bubble marks are a consequence of a poorly sealed toner cartridge or waste toner bin. Loose toner is carried through the printer by the normal motion of the

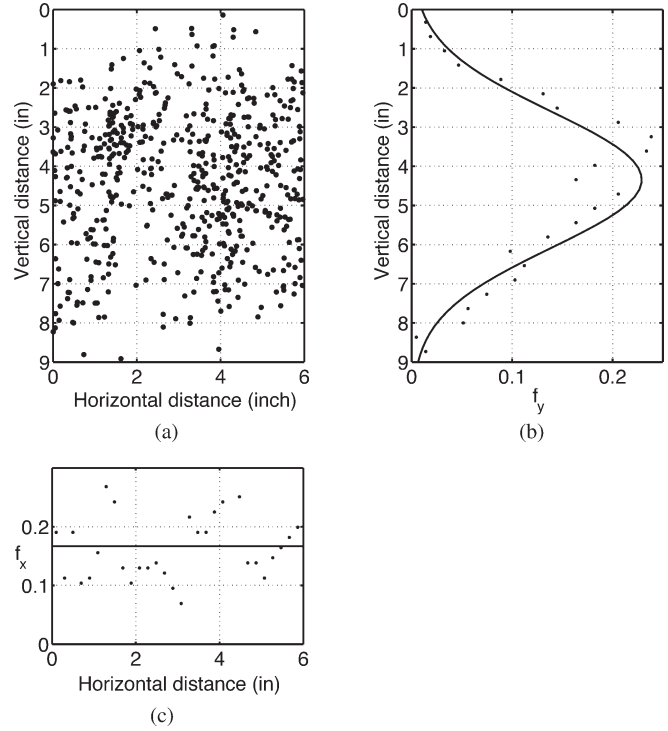


Figure 14. (a) The spatial distribution of scattered white specks acquired from a 6 in \times 9 in sample test page, (b) Gaussian probability density function fitted to the distribution of the vertical positions of the scattered specks ($\mu = 4.34$, $\sigma = 1.74$), and (c) uniform probability density function fitted to the distribution of the horizontal positions of the scattered specks.

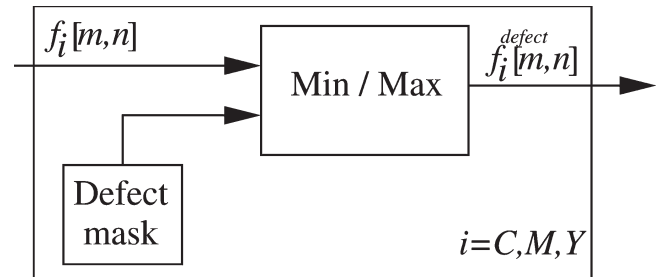


Figure 15. Defect synthesis block for randomly scattered white specks, toner bubbles, repetitive marks, and repetitive bands. The min operator is used for the white specks; and the max operator is used for the other defects.

printer components and is literally splattered onto a roller, drum, belt, or the paper itself. Figure 17 shows a sample of the resulting defect. From a sample print, we observed that the defect marks could be categorized into three distinct groups. For each group, we developed a geometrical model for the shape, plus a procedure for rendering the fill within each shape element. This procedure takes into account the natural graduation of the gray value from the center of the element to its boundary, including the random fluctuation in gray value with respect to spatial position within the element. Because of the complexity of the models for the three types of toner bubble marks, it was necessary to carry out an iterative process in which we used the model to simu-

Paper process direction ←



Figure 16. Image with simulated scattered white speck defect. *Supplemental Material—Figure 16 can be found in color on the IS&T website (www.imaging.org) for a period of no less than two years from the date of publication.*

late marks, visually compared the results with our sample defect marks, revised the model, then resimulated the marks with the revised model, and so on. In the following three subsections, we describe the process for characterizing and simulating each of the three types of toner bubble marks.

Characterization and Simulation for Type I Mark

We illustrate four sample marks of Type I in Fig. 18. Since the Type I marks are nearly round, we model their shape by using a separate segment of an ellipse in each quadrant as shown in Fig. 19. According to this model, the shape of the mark is specified by its width W , height H , and four vertices $(x_1, 0)$, (x_2, H) , $(0, y_1)$, and (W, y_2) .

We acquired 20 sample marks of Type I from a scanned page containing toner bubble marks. We statistically analyzed the distributions of W and H . Based on inspection of the distribution of W , we fitted to the data the Gamma distribution given by Eq. (7). We then used a linear regression to find the height H of the mark as a function of the width W . We also analyzed the distributions of x_1/W , x_2/W , y_1/H , and y_2/H , and fitted Gaussian densities to each of these data sets.

To simulate a mark of Type I, the parameters W , H , x_1 , x_2 , y_1 , and y_2 are generated based on the distributions described above. Then the outline of the mark is delineated using the model shown in Fig. 19. We render the inside of the mark by gradually decreasing the absorptance from the center to the boundary. If we separately render each quarter-ellipse with respect to its own center point, there may be an abrupt change in gray value between neighboring quadrants. In order to obtain a smooth tone variation across the quadrants, we use the same center point $(x_c, y_c) = (W/2, H/2)$ when rendering the fill in all four quadrants. For a given angle θ , we find the point (x_θ, y_θ) on the boundary of the appropriate quarter-ellipse of the mark as shown in Fig. 19. Then for each $\gamma \in [0, 1]$, the coordinate (x, y) of the point on the line connecting (x_c, y_c) and (x_θ, y_θ) is determined according to

$$x = d\gamma \cos(\theta) + x_c, \quad (8)$$

$$y = d\gamma \sin(\theta) + y_c, \quad (9)$$

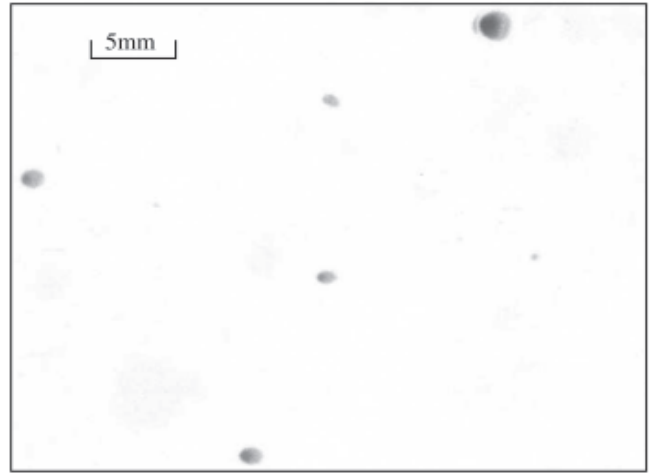


Figure 17. Scanned sample of toner bubbles.



Figure 18. Scanned sample marks of Type I of the toner bubble defect.

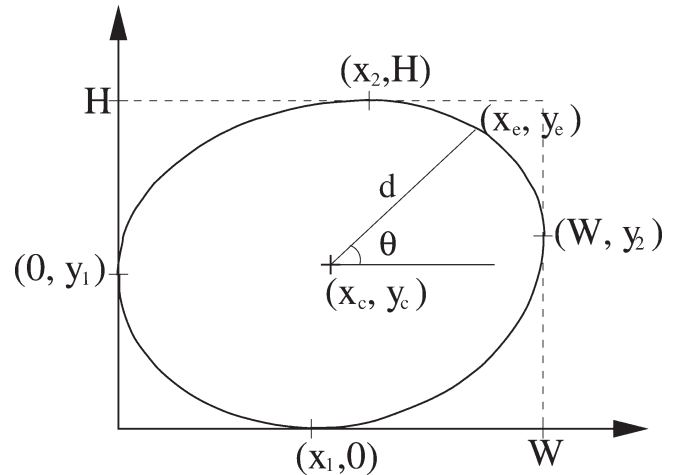


Figure 19. Modeling the shape of the Type I mark of the toner bubble defect by using an arc from a separate ellipse in each quadrant.

where d is the distance between the two points (x_c, y_c) and (x_θ, y_θ) . We render this point with gray value

$$\alpha_\theta(\gamma) = (A/2) (\cos(\gamma\pi) + 1), \quad (10)$$

where A is the gray value at the center point (x_c, y_c) . As γ increases from 0 to 1, $\alpha_\theta(\gamma)$ smoothly decreases from A to 0. In order to model the natural fluctuation in absorptance within the mark, we add filtered random noise to the fill pattern of the simulated defect mark. Figure 20 shows a simulated toner bubble mark of Type I.

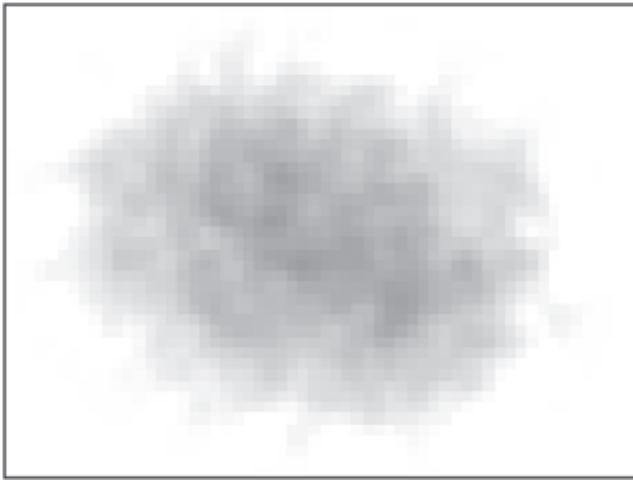


Figure 20. A simulated mark of Type I of the toner bubble defect.

Characterization and Simulation for Type II Mark

Figure 21 shows three samples of Type II marks drawn from our complete set of 15 marks of this kind. While similar to Type I marks, Type II marks are more elongated and contain a distinctly darker inner region that is approximately circular, and which is positioned at the far left edge of the overall mark. We refer to this inner region as the nucleus and the outer region as the coma. Because the marks in our sample set are highly symmetric, we model the nucleus by a circle and the coma by an ellipse as shown in Fig. 22. The vertical coordinates of the centers of both the ellipse and the circle are chosen to be the same. The shape model for the mark is determined by the width W and height H of the ellipse and the center (x_c, y_c) of the circle. Based on our set of 15 sample marks, we fitted a Gaussian density to W and determined H as a function of W using linear regression. We modeled x_c/W as a Gaussian random variable. As shown in Fig. 22, we fixed $y_c = H/2$. The radius of the circle is given by the distance between the left end of the ellipse and the center of the circle. We rendered the inside of the nucleus and the coma using the same technique as that described earlier for rendering the interior of the Type I marks, except that the nucleus is darker. Figure 23 shows a simulated toner bubble mark of Type II.

Characterization and Simulation for Type III Mark

Figure 24 shows two sample Type III defect marks. These marks have the same structure as the Type II marks with the addition of a halo on the left side of the mark. As shown in Fig. 25, our model for the Type III mark is the same as that for the Type II mark, augmented by two half-ellipses to describe the halo area. These half-ellipses are concentric with the nucleus and have minor radii that are the same as that of the coma. Since our printed page containing sample toner bubble defects had only five Type III marks, we could not perform a statistical analysis to estimate the model parameters. Instead, we fitted the model to each of the five marks, and stored the parameters of these marks in a dictionary.

During the simulation process, we randomly choose a set of parameter values from the dictionary. Then we form the defect shape based on the model shown in Fig.



Figure 21. Scanned sample marks of Type II of the toner bubble defect.

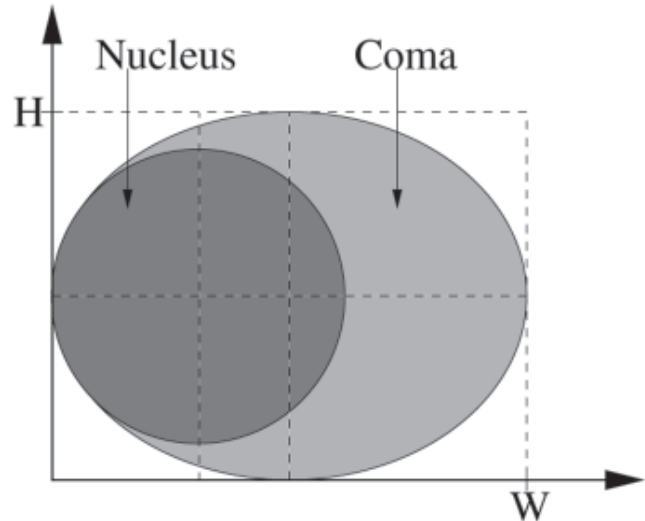


Figure 22. Modeling the shape of the Type II mark of the toner bubble defect.

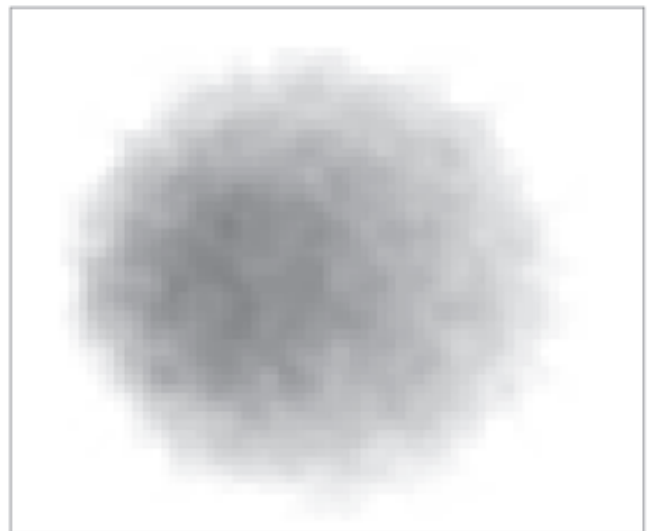


Figure 23. A simulated mark of Type II of the toner bubble defect.

25. The coma and nucleus are rendered in exactly the same way as for Type II marks. We render the halo similarly; but we take into account the fact that the absorbance of the halo is higher at its mid-section than at its tails. Alternatively, we could simply store the actual image of each sample mark, thus basing our simulation

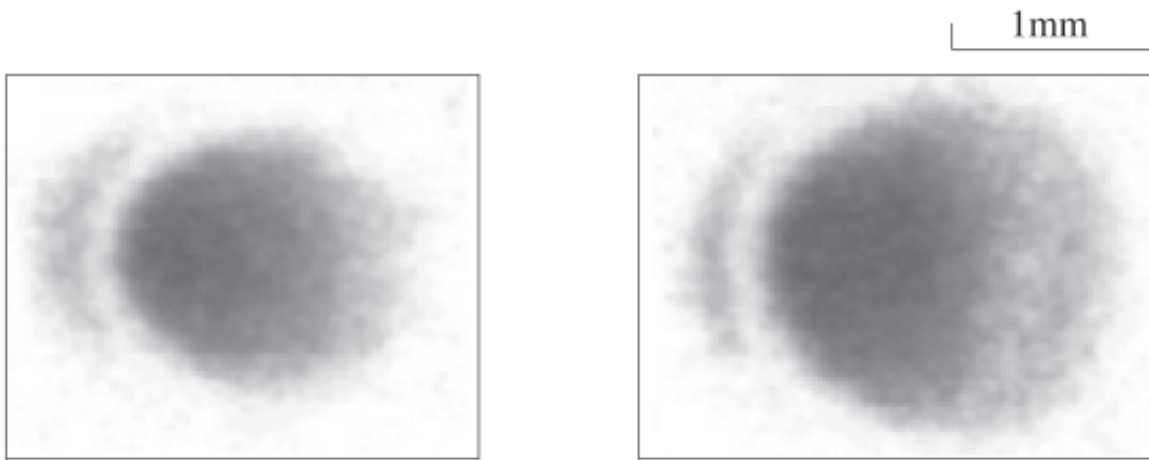


Figure 24. Scanned sample marks of Type III of the toner bubble defect.

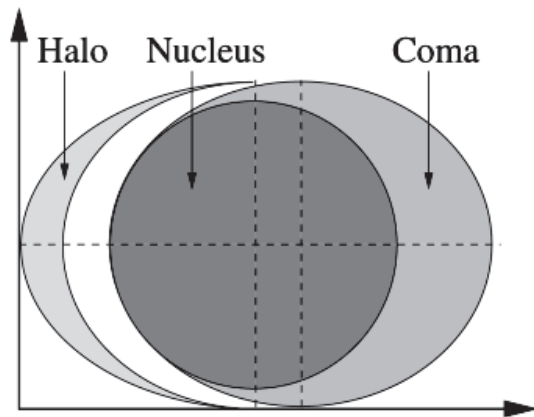


Figure 25. Modeling the shape of the Type III mark of the toner bubble defect.

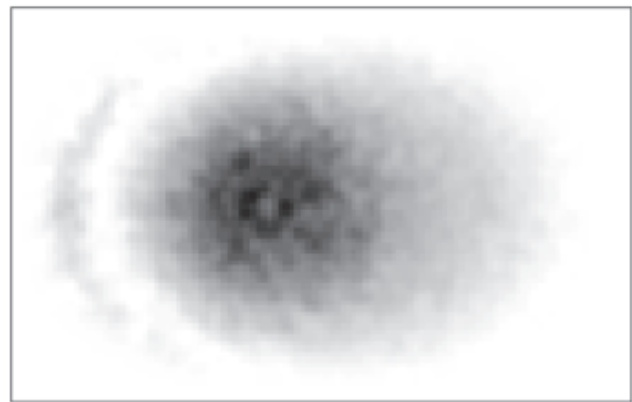


Figure 26. A simulated mark of Type III of the toner bubble defect.

on prototype samples rather than a model. Figure 26 shows a simulated toner bubble mark of Type III.

Simulation Procedure for Toner Bubble Marks

In the simulation procedure, we first determine the total number of defect marks on the page, considering the seriousness of the defect. The number of each type of mark is determined by the ratio of $N_I:N_{II}:N_{III} = 20:15:5$, where N_I is the number of defect marks of Type I. This is based on the number of sample marks of each type that we found on our sample page. Then we independently generate each mark following the previously described procedures. These marks are placed at random on a defect mask that has a white background. Finally, we combine the defect mask with a given input image by using the max operator as shown in Fig. 15. An image with simulated toner bubble marks is shown in Fig. 27.

Repetitive Marks

Repetitive marks are due to localized contamination or damage occurring on the surface of a drum or roller. Because of the contamination or damage, normal imaging cannot take place at this point on the surface of the drum or roller and a localized artifact results. This artifact repeats on the printed page in the process direction with a period given by the circumference of the drum or roller. With a multipass printer, the marks may appear in a sequence of different colors. To generate a defect mark to be inserted in the input image, we use the prototype sample based approach, i.e., we segment defect marks

Paper process direction ←



Figure 27. Image with simulated toner bubbles. *Supplemental Material—Figure 27 can be found in color on the IS&T website (www.imaging.org) for a period of no less than two years from the date of publication.*

from sample images containing defects, and then put them on an input image in the simulation procedure.

Figure 28 shows samples of defect marks, which we manually segmented from the images. In the simulation procedure, a defect mark is separately put on each



Figure 28. Samples of repetitive defect marks.

of the CMY color planes of an input image according to the repeating pattern by using the max operator and a defect mask as shown in Fig. 15. A black mark that might be observed with a CMYK printer can be simulated by putting the same mark at the same location on all CMY planes. Figure 29 shows an image with simulated repetitive CMYK defect marks in a row for a multipass printer with a damaged OPC drum.

Repetitive Coarse-Pitch Bands

Figure 30 shows another type of repetitive defect, which is caused by a defective charging roller. The charging roller is supposed to uniformly charge the surface of the OPC drum before the laser scans the latent image onto it. If the charging roller is held in contact with the OPC drum for a period of time while the printer is idle, the contact area of the charging roller can be flattened. The flattened area will charge the OPC differently than the non-flattened areas. This will modify the development along the length of the OPC, and will result in a band on the print that is perpendicular to the process direction. The band will reoccur in the process direction at an interval equal to the circumference of the charging roller. The repetitive coarse-pitch bands will not be exactly identical, but will have a similar appearance.

Figure 31(a) shows the projected absorbance profile $g[n]$ acquired from an image $g[m,n]$ containing a repetitive band. We note that the profile has the shape of one valley between two peaks. Based on this inspection, we develop a model for the absorbance profile as shown in Fig. 31(b). This profile is described by segments of five different sinusoids with end points $(c_k, d_k), k = 0, 1, \dots, 4$; so

$$\hat{g}[n] = \frac{d_k + d_{k-1}}{2} - \frac{d_k - d_{k-1}}{2} \cos\left(\frac{n - c_{k-1}}{c_k - c_{k-1}} \pi\right), \quad c_{k-1} \leq n \leq c_k. \quad (11)$$

Within each range $c_k - 1 \leq n < c_k$, Eq. (11) connects the two points $(c_k - 1, d_k - 1)$ and (c_k, d_k) with a half cycle of a cosine. In this model, we set d_0 and d_4 to zero.

As can be seen in Fig. 30, the cross-sectional profile of each band varies in the vertical direction along the length of the band. To capture this behavior, we examine the variation in the heights $d_1[m]$ and $d_3[m]$ of the two peaks and the depth $d_2[m]$ of the valley between them as a function of vertical position m along the band. To remove the influence of very low frequency fluctuation in these signals that are not related to the structure of the band itself, we filter $d_k[m], k = 1, 2, 3$ with an ideal highpass filter having its cutoff at 5 cycles/in.

We then measure the correlation between the three filtered signal $\bar{d}_k[m], k = 1, 2, 3$. Since the correlation coefficient for any two of the three signals is less than 0.1, we assume that they are all independent; and we model each one of them separately by using a first or-

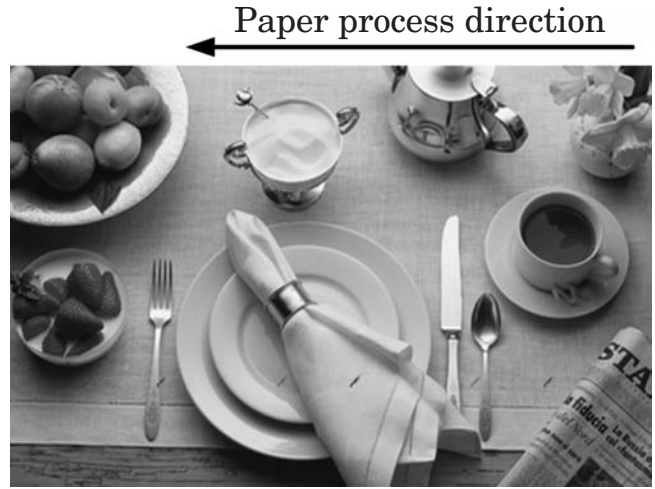


Figure 29. Image with simulated repetitive defect due to damage to the OPC drum of a multipass CMYK printer. A pattern of defective marks in alternating colors repeats across the page in the horizontal (process) direction. *Supplemental Material*—Figure 29 can be found in color on the IS&T website (www.imaging.org) for a period of no less than two years from the date of publication.

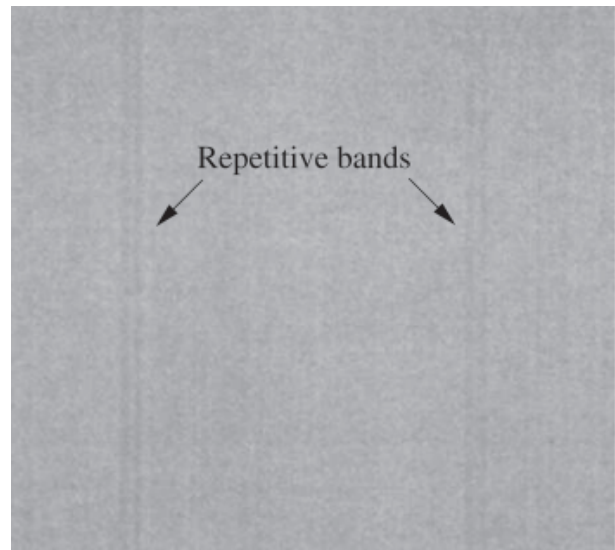


Figure 30. Scanned sample of a repetitive bands defect.

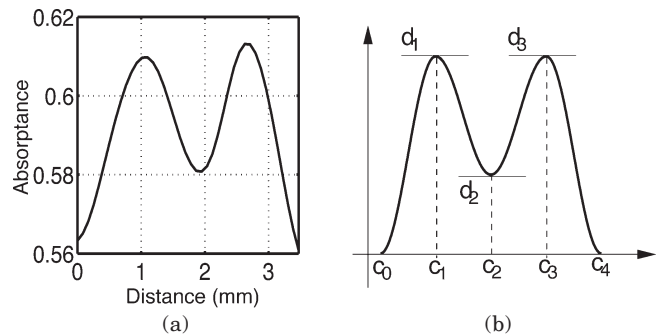


Figure 31. Repetitive bands defect: (a) projected absorbance obtained from scanned defect sample, and (b) piece wise sinusoidal model for the projected absorbance.

der Markov chain,²⁷ which takes on 11 possible states. So we quantize each of the filtered signals to have 11 values. Figure 32 shows an example signal that has been processed in this manner. Since we scan the defect prints at 300 dpi, a unit change in the spatial index in this figure corresponds to 1/300 in.

For each filtered and quantized signal $\tilde{d}_k[m], k=1,2,3$, the Markov chain is specified by the probability state transition matrix \mathbf{P}^k . The (i,j) th element of this matrix is the probability of transition from state i to state j . We estimate these probabilities according to

$$\hat{p}_{ij}^k = \frac{n_{ij}^k}{n_i^k}, \quad (12)$$

where n_{ij}^k is the number of transitions from state i to j in the signal

$$\tilde{d}_k[m], k=1,2,3, \text{ and } n_i^k = \sum_j n_{ij}^k.$$

The steady state probability distribution for the process is given by the vector \bar{p}^k for which the i th element \hat{p}_i^k is the probability of being in state i . This vector is the solution to $\bar{p}^k = \mathbf{P}^k \bar{p}^k$. Its elements can be estimated as

$$\hat{p}_i^k = \frac{n_i^k}{\sum_j n_j^k}. \quad (13)$$

As an example, Eq. (14), shows the estimate obtained for \mathbf{P}^1 .

$$P^1 = \begin{pmatrix} .667 & .333 & 0 & 0 & 0 & 0 & 0 & 0 & 0 & 0 & 0 \\ .143 & .429 & .429 & 0 & 0 & 0 & 0 & 0 & 0 & 0 & 0 \\ 0 & .059 & .686 & .255 & 0 & 0 & 0 & 0 & 0 & 0 & 0 \\ 0 & 0 & .094 & .703 & .196 & .007 & 0 & 0 & 0 & 0 & 0 \\ 0 & 0 & 0 & .154 & .639 & .201 & .006 & 0 & 0 & 0 & 0 \\ 0 & 0 & 0 & .011 & .188 & .597 & .205 & 0 & 0 & 0 & 0 \\ 0 & 0 & 0 & 0 & .008 & .273 & .462 & .250 & .008 & 0 & 0 \\ 0 & 0 & 0 & 0 & 0 & 0 & .241 & .645 & .113 & 0 & 0 \\ 0 & 0 & 0 & 0 & 0 & 0 & 0 & .347 & .531 & .122 & 0 \\ 0 & 0 & 0 & 0 & 0 & 0 & 0 & 0 & .353 & .588 & .059 \\ 0 & 0 & 0 & 0 & 0 & 0 & 0 & 0 & 0 & .250 & .750 \end{pmatrix} \quad (14)$$

For this state transition matrix, the probability distribution of the states is given by

$$\bar{p}^1 = [.004 .008 .058 .155 .190 .198 .149 .159 .055 .019 .005]^t, \quad (15)$$

where the superscript t denotes transpose.

To synthesize each signal $\hat{a}_k[m], k=1,2,3$ according to its Markov chain model \mathbf{P}^k , we set $m=0$ and choose an initial state i according to the probability distribution vector \bar{p}^k . We then increment m and generate a new state j according to the probability distribution given by the i th row of \mathbf{P}^k . We repeat this process until $m=M-1$, where M is the length of the desired signal. For our random number generator, we use the function $rand()$ in the Linux C library.²⁸ Given the signals $\hat{a}_k[m], k=1,2,3$, we use Eq. (11) to synthesize the band cross-

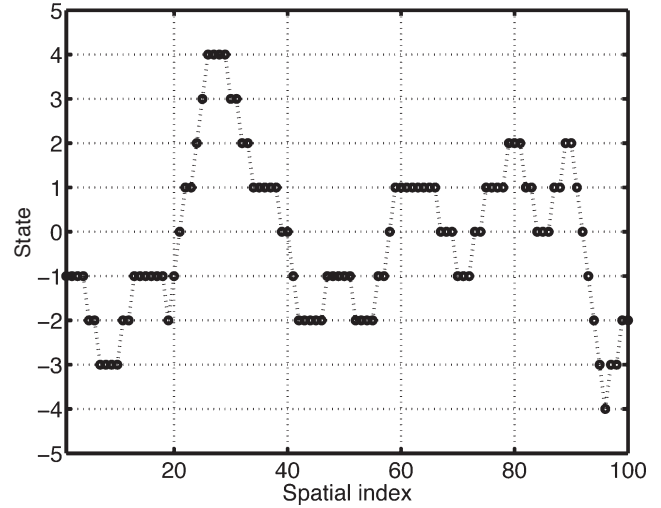


Figure 32. State transition plot for a 1/3 in vertical segment of the quantized height $d_1[m]$ of the first peak in the absorbance profile.

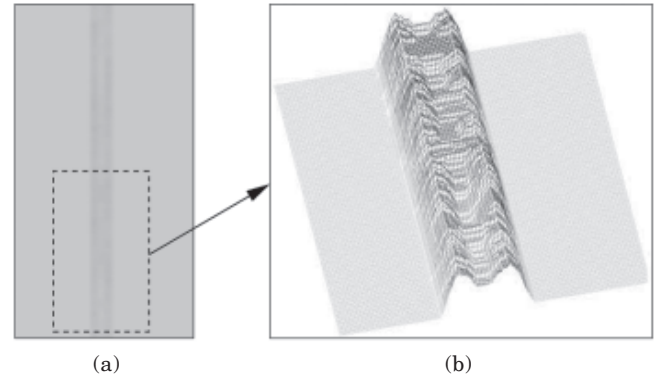


Figure 33. (a) Simulation of a defective band on a gray image, and (b) a three dimensional plot for part of the simulated band.

section at each position m . This entire process is repeated for each of the bands that is to be synthesized on the page.

In Fig. 33, we show a repetitive band defect simulated on a constant tone image and a 3D plot for part of that band. From the 3D plot, we observe that the absorbance profile has the double-arch shape shown in Fig. 31(b). Comparing Figs. 30 and 33(a), we see that our model captures the natural variation in the appearance of the cross-section along the length of the band. We combine the defect mask $b_i[m,n]$ and the input image $f_i[m,n]$ according to

$$f_i^{bands}[m,n] = f_i[m,n] + \rho_i b_i[m,n], \quad (16)$$

where ρ_i is the parameter controlling the defect level and $i=C, M$, and Y . An image with a simulated repetitive band defect in the magenta plane is shown in Fig. 34.

Ghosting

Ghosting is a PQ defect showing a dimly repeated image at an interval in the paper process direction as indicated in Fig. 35. The source of ghosting is residual toner particles on the surface of a printer unit such as an OPC

Paper process direction



Figure 34. Image with simulation of repetitive bands defect. *Supplemental Material—Figure 34 can be found in color on the IS&T website (www.imaging.org) for a period of no less than two years from the date of publication.*

Paper process direction

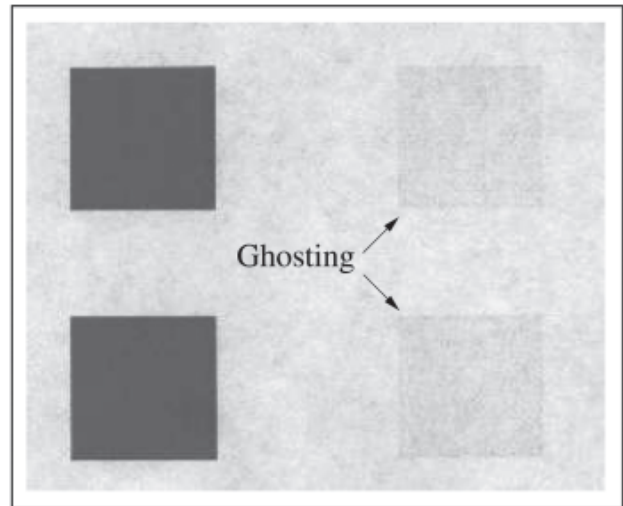


Figure 35. A scanned sample with a ghosting defect.

drum or a fuser roller.^{12,13} If a cleaning unit does not work properly, toner particles remaining from the previous image will be transferred onto the paper, thereby generating a ghost image. The strength of ghosting can be measured with a test page consisting of a source pattern and a constant tone field displaced from the source pattern in the process direction by a distance equal to the circumference of the component responsible for ghosting. Reference 12 proposes such a test page, in which the source pattern consists of a series of black rectangular bars; and the background field is filled with a 50% tone. However, the ghost image is more clearly visible when the tone of the source image is darker, and the tone of the background where the ghost shows up is lighter. In other words, the severity of ghosting depends on the tone level of both the source image and that of the background.

In order to investigate the tone dependency of ghosting, we developed a set of test target pages to quantify this phenomenon. Figure 36 shows one of these pages. In our test target pages, we employ a sinusoidal waveform. We call this sinusoidal waveform which induces the ghosting defect the *source pattern*. We call the set of constant tone bars where ghosting appears the *background field*. We measured the ghosting tone dependency by examining how clearly the ghosting defect appears on the background field at various tone levels while changing the tone level of the source pattern.

Let a^b and a^s be the normalized digital values of the background field and the source pattern, respectively. We use six different tone levels for the background field: $a^b = 0.0, 0.2, 0.4, 0.6, 0.8,$ and 1.0 . For a given test target page, we fixed the amplitude and the bias of the source pattern signal as

$$s_{a^s}[m] = \frac{a^s}{2} [\sin(2\pi v_g m / R) - 1]. \quad (17)$$

Here R is the resolution at which the test target page is printed. We use five different tone levels $a^s = 0.2, 0.4, 0.6, 0.8,$ and 1.0 for the source pattern, each of which is printed on a different page. We set the frequency of the source pattern signal to $v_g = 2$ cycles/in.

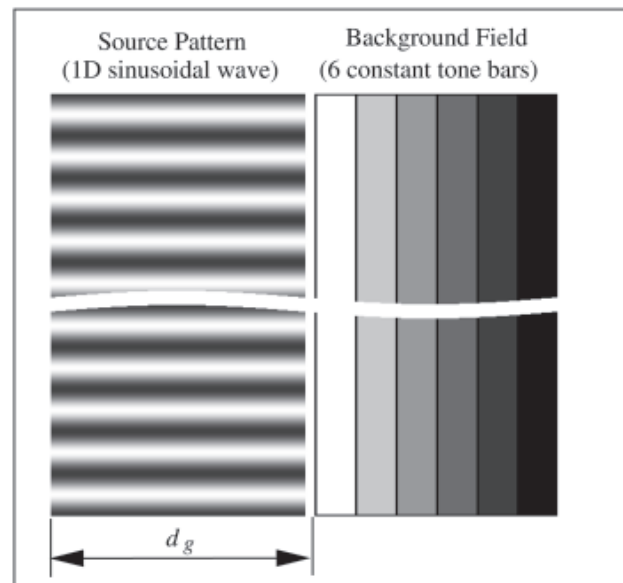


Figure 36. Test target page used to measure ghosting tone dependency. When the page is printed with a defective printer, the source pattern will be dimly repeated on the background field showing ghosting at an interval d_g .

To obtain the Ghosting Tone Dependency Function (GTDF), we first calculate the FFT magnitude at v_g for each pair (a^s, a^b) from the scanned test target page, and interpolate the data points. Then we normalize the interpolated data so that the GTDF $h^g(a^s, a^b)$ has a maximum value of one. Figure 37 shows the ghosting tone dependency for the M plane. As discussed earlier, the strength of ghosting increases with the absorbance of the source and decreases with the absorbance of the background. By utilizing the GTDF, we devise a ghosting simulation model as

$$f_i^{\text{ghosting}}[m, n] = f_i[m, n] + \rho_i h^g(f_i[m, n - d_g], f_i[m, n]), \quad (18)$$

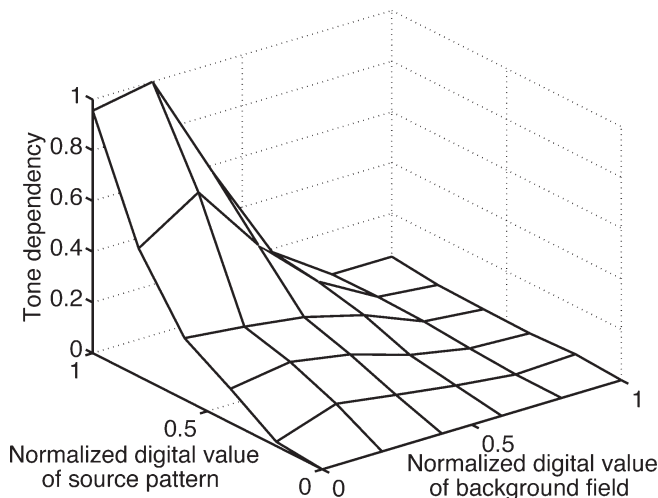


Figure 37. Measurement of ghosting tone dependency for the M plane.

where d_g is the ghosting interval, ρ_i is the parameter controlling the defect level, and $i = C, M,$ and Y . Figure 38 illustrates the ghosting synthesis block for this model. An image with simulated ghosting is shown in Fig. 39. Here the front part of the airplane is dimly repeated on the light tone area.

Simulation of Color Defects

The subject of this entire article has been simulating print quality defects observed with color laser printers; so to entitle a section *Simulation of Color Defects* may seem to be not particularly descriptive. However, all of the defects discussed so far can be seen separately in each of the color planes and could, in fact, also be observed, albeit with different appearance, on pages printed with a monochrome laser printer. In contrast, what we mean by *color defects* are those defects that can only be seen as a result of the interaction between different color planes. These defects have no meaning in the context of a monochrome printer. There are two such defects that are especially common with color laser printers. The first defect is failure of color plane registration; and the second one is temporal inconsistency. We consider them separately in the following two subsections.

Failure of Color Plane Registration

With every laser printer architecture, the color planes are developed sequentially and built up plane-by-plane on an intermediate transfer drum or belt, or on the paper itself. Therefore, the accuracy with which the different color planes are placed on top of each other is a key issue for a color laser printer. Poor performance of color plane registration (CPR) can result in a print that looks out of focus. Text that consists of two or more primary color planes will seem to have halo around it, as shown in Fig. 40. Figure 41 shows our procedure for simulating a CPR defect. The defect is completely characterized by three translation vectors $t_i = (m_i^i, n_i^i), i = C, M, Y$, which have units of pixels. These vectors determine the direction and the extent of misregistration of the color planes. We separately apply the translation vectors to each of the CMY planes according to

$$f_i^{CPR}[m,n] = f_i[m + m_i^i, n + n_i^i], \quad (19)$$

where $i = C, M,$ and Y . Figure 42 shows an original image and the same image with a simulated CPR defect.

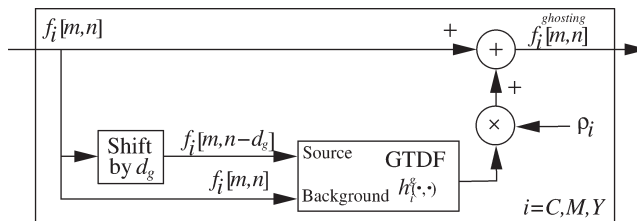


Figure 38. Ghosting synthesis block for a color image.



Figure 39. Image with simulated ghosting defect. The front part of the airplane is dimly repeated on the light tone area. *Supplemental Material*—Figure 39 can be found in color on the IS&T website (www.imaging.org) for a period of no less than two years from the date of publication.

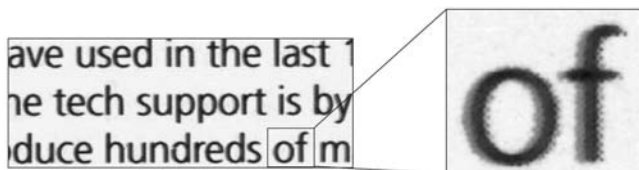


Figure 40. A scanned sample exhibiting color plane misregistration.

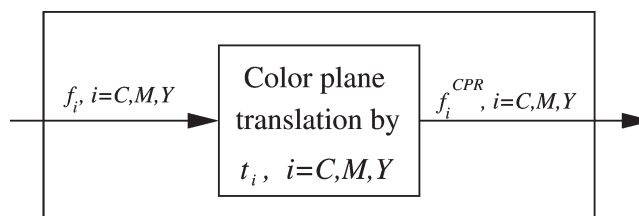


Figure 41. CPR defect synthesis for a color image.

Temporal Color Inconsistency

The temporal color inconsistency is caused by changes over time in the relationship between colorant density printed on the page and input digital value for one or more colorant planes. We refer to this relationship as the tone reproduction curve (TRC), and denote it by $T_i(a)$,

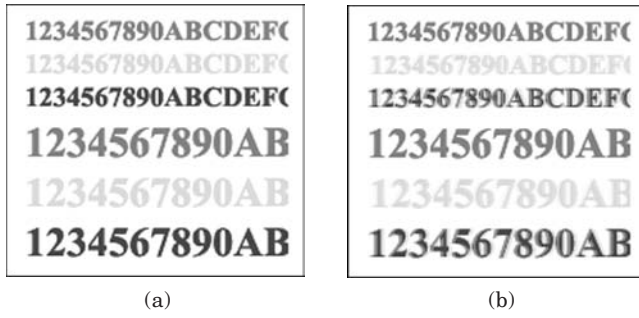


Figure 42. Simulation of CPR defect: (a) original image, and (b) image with simulated CPR defect. The C plane is shifted to right by 2 pixels at 150 dpi ($\approx 350 \mu\text{m}$). *Supplemental Material—Figure 42 can be found in color on the IS&T website (www.imaging.org) for a period of no less than two years from the date of publication.*

$i = C, M, \text{ or } Y$, where \mathcal{T}_i is the density and a is the normalized digital value. Although temporal changes in the TRC are also possible with a monochrome printer, the degree of change that will be problematic for a color printer is likely to be perfectly acceptable with a monochrome printer. This is because with a monochrome printer, we would observe small variations in the gray level of tint fill patterns. With a color printer, even small changes in the TRC can produce unacceptable shifts in hue. So as with the defect of color plane registration, the interaction between different color planes plays a critical role in the temporal color inconsistency.

Figure 43 illustrates the defect of temporal color consistency for a real printer. It shows scanned versions of two step wedges printed with the same color printer at times 17 hours apart. The lowest density step corresponds to digital value 0 which should result in no colorant as is correctly shown in both wedges. However, the next two steps (Nos. 2 and 3) corresponds to non-zero digital values. The wedge for Dataset A (Fig. 43(a)) does indeed show colorant development for these two steps; whereas the wedge for Dataset B (Fig. 43(b)) does not.

This effect may be quantified by the TRC's for this printer at these two points in time, which can be determined by simply measuring the density values of each patch in Fig. 43 with a Gretag SPM50 (Gretag, Chicopee, MA, 01022), and fitting a curve to the data as shown in Fig. 44. Here, as expected, the TRC for Dataset A increases monotonically from density 0 to 1.38 for Patches 1 through 12; while for Dataset B it stays at density 0 for Patches 1, 2, and 3, and then increases monotonically to density 1.34.

To simulate this defect, let us consider a defect of temporal color consistency in the i^{th} color plane $i = C, M, \text{ or } Y$. Let $\mathcal{T}_i^n(a)$ denote the nominal or correct TRC and $\mathcal{T}_i^d(a)$ denote the TRC for a printer with a defect of temporal color consistency. Our goal is to find a tone modification curve $X_i(a)$ which when applied to the image prior to printing on a printer with TRC $\mathcal{T}_i^n(a)$ will yield an effective TRC $\mathcal{T}_i^d(a)$. Thus we require that

$$\mathcal{T}_i^d(a) = \mathcal{T}_i^n(X_i(a)). \quad (20)$$

Assuming that

$$\min_{0 \leq a \leq 1} \mathcal{T}_i^n(a) \leq \min_{0 \leq a \leq 1} \mathcal{T}_i^d(a), \quad (21)$$

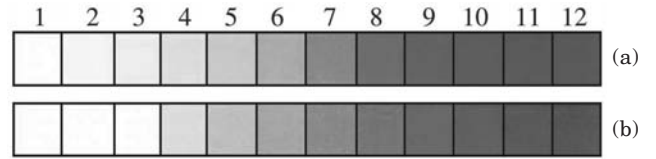


Figure 43. Two scanned sets of cyan color patches, showing the problem of temporal color inconsistency. These two sets were printed with the same color laser printer at an interval of 17 hours. *Supplemental Material—Figure 43 can be found in color on the IS&T website (www.imaging.org) for a period of no less than two years from the date of publication.*

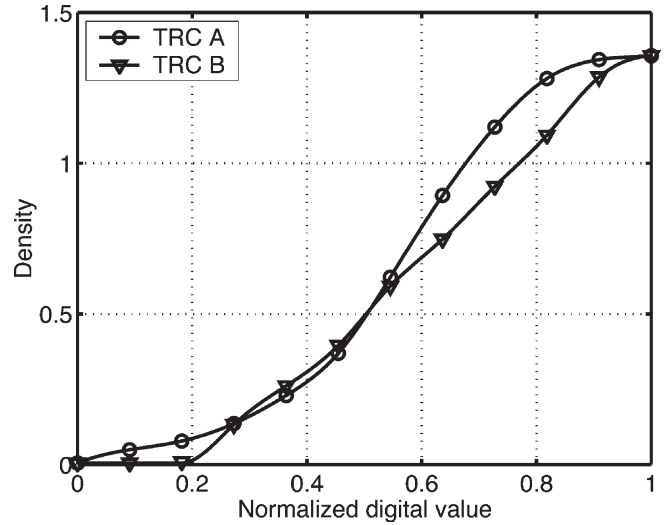


Figure 44. Tone reproduction curves fitted to the data sets A and B. The two data sets were acquired by measuring the density values of the color patches shown in Fig. 43.

and

$$\max_{0 \leq a \leq 1} \mathcal{T}_i^n(a) \geq \max_{0 \leq a \leq 1} \mathcal{T}_i^d(a), \quad (22)$$

and that $\mathcal{T}_i^n(a)$ is monotonically increasing in a for $0 \leq a \leq 1$, we have that

$$X_i(a) = \left(\mathcal{T}_i^n\right)^{-1}\left(\mathcal{T}_i^d(a)\right). \quad (23)$$

As an illustration, Fig. 45 shows the tone modification curve $X_i(a)$ for the cyan plane when the nominal and defective TRC's are based on Datasets A and B, respectively, in Fig. 44.

Once we have the tone modification curves $X_i(a)$, $i = C, M, Y$ for each color plane, we can simulate a defect of temporal color consistency according to the diagram in Fig. 46. The tone modification functions are separately applied to each of the CMY planes according to

$$f_i^{\text{consist}}[m, n] = X_i(f_i[m, n]), \quad (24)$$

where $i = C, M, Y$. The defect of temporal color consistency is simulated in Fig. 47. Figure 47(a) is an image which we assume is rendered by the desired nominal TRC for each color plane. On the other hand, Fig. 47(b)

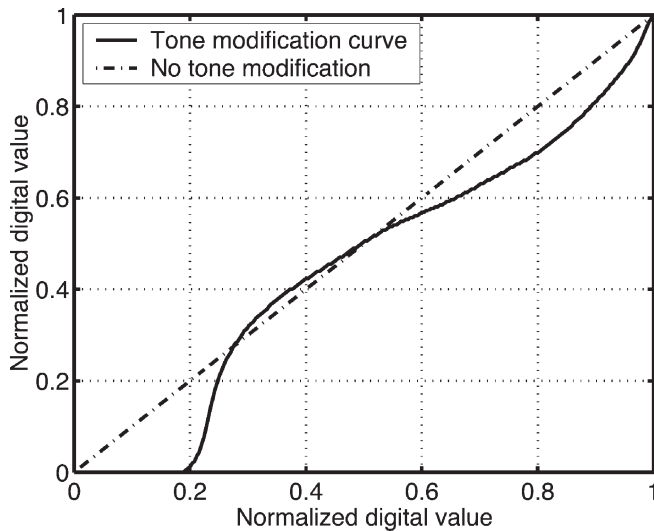


Figure 45. Tone modification curve derived from the two TRC's shown in Fig. 44 by using Eq. (23).

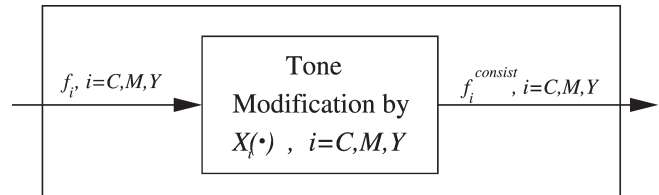


Figure 46. Defect synthesis block for temporal color inconsistency.



(a)



(b)

Figure 47. Simulation of defect of temporal color consistency: (a) original image, and (b) image showing simulated defect of color consistency. The C plane is modified by the tone modification curve shown in Fig. 45 and shows up in the graphic representation above as an apparent reduction in contrast. *Supplemental Material*—Figure 47 can be found in color on the IS&T website (www.imaging.org) for a period of no less than two years from the date of publication.

is a simulated image with a defective TRC for the cyan plane. For this simulation, we used the tone modification curve shown in Fig. 45.

Conclusion

Simulation of print quality defects is important to several aspects of providing service and support for color printers, especially next-generation strategies for improving the customer experience and reducing the cost to the manufacturer. We have developed a general framework for simulation of print quality defects, and shown how concepts from signal processing, geometry, and stochastic processes can be brought bear on the problem of creating photorealistic renderings of print quality defects. We describe methods for simulating defects in three broad categories: defects of uniformity, random marks or repetitive artifacts, and color defects. Each defect is simulated through a stochastic model based approach, or by using a prototype defect sample. For the model based approach, the parameters are esti-

mated from scanned samples of actual print defects. For the prototype sample-based approach, a scanned sample of the defect is used as the prototype. In each case, we are able to obtain a very realistic rendering of the target defect.

It is also very important to measure the goodness of the simulated defects. Ultimately, the simulated defect should be close to the real defect printed from a defective printer. How we assess the degree of closeness may depend on the intended application. For example, if the simulations are to be viewed by customers to assist in diagnosis of their PQ defects, then it may be appropriate to conduct psychophysical tests in which we measure the ability of subjects to distinguish between real and simulated defects. On the other hand, if the simulations are to be used in the development of algorithms for automatic detection and identification of PQ defects, quantitative metrics for image similarity may be more appropriate. In any case, developing a meaningful assessment of the goodness of any type of simulated de-

fect is not a simple task, and would be a worthy goal for future research. ▲

Acknowledgment. We would like to thank the Hewlett-Packard Company for supporting this research. We would like to express our sincere gratitude to Tony Barrett and Rich Payne for their interest and encouragement during this project.

References

1. W. Jang, M. Chen, G. T. C. Chiu, and J. P. Allebach, Print quality test page, in *Proc. IS&T's NIP 19: International Conference on Digital Printing Technologies*, IS&T, Springfield, VA, 2003, pp. 575–580.
2. S. Leman and M. R. Lehto, Interactive decision support system to predict print quality, *Ergonomics* **46**, 52–67 (2003).
3. Y. Bang, Z. Pizlo, J. P. Allebach, and N. Burningham, Discrimination based banding assessment, in *Proc. IS&T's NIP 19: International Conference on Digital Printing Technologies*, IS&T, Springfield, VA, 2003, pp. 745–750.
4. M. Sampath, R. Rockwell, D. R. Rasmussen, A. Godambe, E. Jackson, and R. Minhas, Automated banding defect analysis and repair for document processing systems, US Pat. Application 20030142985, 2003 (assigned to Xerox Co.).
5. P. W. Melnychuck, Fourier spectra of digital halftone images containing dot-position errors, *J. Opt. Soc. Amer.* **5**, 1328–1338 (1988).
6. B. Mishra and D. R. Rasmussen, Microuniformity: An image quality metric for measuring noise, in *Proc. IS&T PICS 2000: Image Processing, Image Quality, Image Capture, Systems Conference*, IS&T, Springfield, VA, 2000, pp. 75–78.
7. R. P. Loce, W. L. Lama, and M. S. Maltz, Modeling vibration-induced halftone banding in a xerographic laser printer, *J. Electronic Imaging* **4**, 48–61 (1995).
8. P. J. Kane, T. F. Bouk, P. D. Burns, and A. D. Thompson, Quantification of banding, streaking and grain in flat field images, in *Proc. IS&T PICS 2000: Image Processing, Image Quality, Image Capture, Systems Conference*, IS&T, Springfield, VA, 2000, pp. 79–83.
9. G.-Y. Lin, J. M. Grice, J. P. Allebach, G. Chiu, W. Bradburn, and J. Weaver, Banding artifact reduction in electrophotographic printers by using pulse width modulation, *J. Imaging Sci. Technol.* **46**, 326–337 (2002).
10. P. D. Burns, M. Rabhani and L. A. Ray, Analysis of image noise due to position errors in laser writer, *Applied Optics* **25**, 2158–2168 (1986).
11. H. Mizes, N. Goodman and P. Butterfield, The perceptibility of random g streaking, in *Proc. IS&T PICS 2000: Image Processing, Image Quality, Image Capture, Systems Conference*, IS&T, Springfield, VA, 2000, pp. 89–93.
12. J. C. Briggs, E. Hong, and D. Forrest, Analysis of ghosting in electrophotography, in *Proc. IS&T's NIP 16: International Conference on Digital Printing Technologies*, IS&T, Springfield, VA, 2000, pp. 403–407.
13. P. L. Jeran and N. Burningham, Measurement of electrophotographic ghosting, in *Proc. IS&T PICS 2001: Image Processing, Image Quality, Image Capture, Systems Conference*, IS&T, Springfield, VA, 2001, pp. 80–83.
14. P. J. Kane and R. E. Cookingham, A color grain ruler for the measurement of print graininess, in *Proc. IS&T PICS 1998: Image Processing, Image Quality, Image Capture, Systems Conference*, IS&T, Springfield, VA, 1998, pp. 192–195.
15. R. N. Strickland, Tumor detection in nonstationary backgrounds, *IEEE Transactions on Medical Imaging* **13**, 491–499 (1994).
16. C. Davatzkitos, D. Shen, A. Mohamed, and S. K. Kyriacou, A framework for predictive modeling of anatomical deformations, *IEEE Trans. Med. Imaging* **20**, 836–843 (2001).
17. D. S. Paik, C. F. Beaulieu, G. D. Rubin, B. Acar, B. Jeffrey, J. Yee, J. Dey, and S. Napel, Surface normal overlap: A computer-aided detection algorithm with application to colonic polyps and lung nodules in helical CT, *IEEE Trans. Med. Imaging* **23**, 661–675 (2004).
18. J. S. Lim, *Two-Dimensional Signal and Image Processing*, Prentice Hall, Upper Saddle River, NJ, 1990.
19. M. R. Banham and A. K. Katsaggelos, Digital image restoration, *IEEE Signal Processing Magazine* **14**, 24–41 (1997).
20. A. K. Jain, *Fundamentals of Digital Image Processing*, Prentice Hall, Upper Saddle River, NJ, 1989.
21. T. L. Williams and T. Wojtowicz, Optical measurements-current challenges, in *Proc. IEE Colloquium on Recent Advances in Broadcast TV Cameras – Optics, Sensors and Processing*, IEE, London, UK, 1991, pp. 1–6.
22. J. Garcia, J. M. Sanchez, X. Orriols, and X. Binefa, Chromatic aberration and depth extraction, in *Proc. Pattern Recognition*, IEEE, Los Alamitos, CA, 2000, pp. 762–765.
23. D. Kacker, T. Camis and J. P. Allebach, Electrophotographic process embedded in direct binary search, *IEEE Trans. Image Processing* **11**, 243–257 (2002).
24. C.-L. Chen, G. T.-C. Chiu and J. Allebach, Banding reduction in electrophotographic process using human contrast sensitivity function shaped photoreceptor velocity control, *J. Imaging Sci. Technol.* **47**, 209–223 (2003).
25. J. G. Proakis and D. G. Manolakis, *Digital Signal Processing: Principles, Algorithms, and Applications*, 3rd ed., Prentice Hall, Upper Saddle River, NJ, 1996.
26. D. Rasmussen, E. N. Dalal and K. M. Hoffman, Measurement of macro-uniformity: streaks, bands, mottle and chromatic variations, in *Proc. IS&T PICS 2001: Image Processing, Image Quality, Image Capture, Systems Conference*, IS&T, Springfield, VA, 2001, pp. 90–95.
27. S. M. Ross, *Stochastic Processes*. 2nd ed., John Wiley & Son, Inc., New York, NY, 1996.
28. ISO/IEC/JTC1/SC22/WG14, *International standard for programming language C*, ISO/IEC 9899, 1999.